JOURNAL OF SYNCHROTRON RADIATION

ISSN 1600-5775

Received 9 June 2016
Accepted 29 August 2016

Edited by G. E. Ice, Oak Ridge National Laboratory, USA

Keywords: Laue microdiffraction; nanowire; *in situ* mechanical test; atomic force microscope.

Supporting information: this article has supporting information at journals.iucr.org/s

KB scanning of X-ray beam for Laue microdiffraction on accelero-phobic samples: application to *in situ* mechanically loaded nanowires

C. Leclere,[a] T. W. Cornelius,[a]* Z. Ren,[a] O. Robach,[b,c] J.-S. Micha,[b,d] A. Davydok,[a] O. Ulrich,[b,c] G. Richter[e] and O. Thomas[a]

[a]Aix Marseille Université, CNRS, Université de Toulon, IM2NP UMR 7334, 13397 Marseille, France, [b]CRG-IF BM32 Beamline at the European Synchrotron, CS40220, 38043 Grenoble Cedex 9, France, [c]Université Grenoble Alpes, CEA/INAC/MEM, 17 rue des Martyrs, 38054 Grenoble, France, [d]Université Grenoble Alpes, CEA/INAC, UMR CNRS SPrAM, 17 rue des Martyrs, 38054 Grenoble, France, and [e]Max Planck Institute for Intelligent Systems, Heisenbergstrasse 3, 70569 Stuttgart, Germany. *Correspondence e-mail: thomas.cornelius@im2np.fr

A mapping technique has been developed where a sub-micrometer focused polychromatic X-ray beam is scanned across a stationary sample instead of scanning the sample in front of the X-ray microbeam. This method is applied to a gold nanowire during its mechanical loading using the tip of an atomic force microscope. During the loading process, such a sample is 'accelero-phobic', *i.e.* the sample scanning stages must not to be moved to avoid parasitic additional load. Without beam scanning, only one single position within the sample can be probed during the test. The probed material point may even change because of drifts or movements induced by the test itself. The new scanning approach facilitates the *in situ* mapping of the entire wire giving access to the evolution of the wire shape as well as to the boundary conditions. This novel scanning technique opens promising perspectives for studies where sample motion is forbidden because of the sample environment.

1. Introduction

Among the challenges in the evaluation of mechanical properties at the nanoscale are the development of reliable mechanical tests and the ability to map the inhomogeneous reaction of the sample *in situ*. Several quantities of interest such as the sample shape, the displacement field, the crystal lattice strain field and orientation field may be mapped by different characterization techniques such as scanning electron microscopy (SEM) (Uchic *et al.*, 2004; Kiener *et al.*, 2008), digital image correlation combined with SEM (Richter *et al.*, 2009; Chen *et al.*, 2012), Laue microdiffraction (Chung & Ice, 1999), transmission electron microscopy (Lee *et al.*, 2014) or high-angular resolution electron backscatter diffraction (Konijnenberg *et al.*, 2015). In the recent past, synchrotron-based X-ray diffraction methods received more and more attention with the further development of both the synchrotron sources and the focusing optics [chromatic (Snigirev *et al.*, 1996; Jefimovs *et al.*, 2007) or achromatic (Kirkpatrick & Baez, 1948)] which allow the generation of hard X-ray beams of a few hundred nanometers in size. These highly focused and brilliant X-ray beams facilitate the study of individual nanostructures and the mapping of the displacement field by coherent Bragg diffraction imaging or the orientation field using Laue microdiffraction.

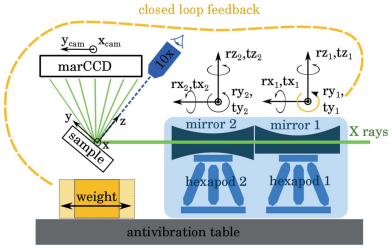

However, regarding *in situ* micro- and nano-mechanical tests in combination with X-ray diffraction techniques, the various testing devices [such as indenters and custom-built atomic force microscopes (AFMs) (Kirchlechner *et al.*, 2012; Marichal *et al.*, 2013; Maaß *et al.*, 2009; Scheler *et al.*, 2009; Rodrigues *et al.*, 2009; Ren *et al.*, 2014; Leclere *et al.*, 2015)] developed so far are essentially accelero-phobic, *i.e.* accelerations may lead to the destruction of the sample. The specimen is usually rigidly fixed to the sample stage, whereas the heavier loading device is mounted *via* a spring-like stress gauge. Consequently, the sample directly follows the movements of the stage whereas the motion of the loading device is delayed resulting in a potentially destructive relative motion of the gripping/pushing device with respect to the specimen. Therefore, sample-stage mapping of the micro- or nano-structures are prohibited during the mechanical loading and, thus, the X-ray beam probes a singular position within the sample.

The present work demonstrates a new mapping technique where a sub-micrometer focused polychromatic X-ray beam is scanned across the sample instead of scanning the sample in front of the fixed X-ray beam. This technique takes advantage of the presence of a hexapod under each of the two Kirkpatrick–Baez (KB) focusing mirrors (Kirkpatrick & Baez, 1948) on the Laue microdiffraction setup installed at the CEA-CNRS CRG-IF BM32 beamline at ESRF (Ulrich, 2012–2015). The two hexapods facilitate the independent positioning of each mirror enabling the two-dimensional displacement of the focused X-ray beam and, thus, the two-dimensional cartography of the sample. This technique is applied to an Au nanowire which is mechanically loaded *in situ* in a three-point bending configuration using the custom-designed AFM 'SFINX' (Ren *et al.*, 2014; Leclere *et al.*, 2015). The beam-scanning range allows for mapping the entire wire giving access to the boundary conditions (doubly clamped or simply supported, *i.e.* resting on only two points), which are of major importance for understanding the mechanical behavior of the nanostructure.

2. Experimental

2.1. Experimental setup at BM32 beamline

The experiments were performed on the French CRG-IF beamline BM32 at the European Synchrotron (ESRF) in Grenoble (France) (Ulrich *et al.*, 2012–2015, 2011). The Laue microdiffraction setup is schematically depicted in Fig. 1. The polychromatic X-ray beam, which covers an energy range of 5 to 23 keV, is focused down to 300 nm horizontally and to 500 nm vertically (parallel to the sample surface) using KB mirrors. Both mirrors were illuminated at an incident angle of about 2.8 mrad. The acceptances for the vertical and the horizontal mirror were set to 0.6 mm (V) × 0.15 mm (H) (compared with a full acceptance of 0.7 mm × 0.3 mm). Figs. S(1*a*) and S(1*b*) of the online supporting information show the footprint of the beam on the surface of the two mirrors in the 'best focus' configuration. Horizontally, the beam full width at half-maximum (FWHM) in front of the slits is 0.14 mm, as imposed by the bending-magnet source size viewed through the pinhole-like secondary slit (23.5 m upstream); hence the use of a 0.15 mm-gap horizontal slit. Best focus is obtained using the downstream half of the second mirror. Each mirror is mounted on a separate hexapod (SYMETRIE®) that allows for six-axes positioning with a precision of 0.1 µm and 2 µrad on the associated translation and angular pseudo-motors. The slit settings limit the range for the mirror motion to [−0.05, +0.05 mm] along the motor tz_1 before the beam touches the mirror edges. For the second (horizontally focusing) mirror, the ty_2 range without intensity loss is [0, +0.15 mm].

In order to limit the transmission of the floor vibrations to the setup, and therefore stabilize the relative positions of the different elements (focusing optics, sample, microscope, X-ray beam), the setup (except for the two-dimensional detector) is mounted on an active vibration-damping plate. The usage of such a vibration-damping plate is rather unusual as a support for optical elements shaping a synchrotron beam. Owing to the spring-like mechanical link between the plate and its supporting frame, any displacement of the center of gravity of the ensemble supported by the plate causes a tilt of the setup. Here, in particular, moving the sample scanning stages or retracting the microscope strongly modifies the tilt of mirror 1 around ry_1, causing a vertical displacement of the micro-beam and a degradation of the vertical size of the beam. A feedback loop driving counter weights (Ulrich *et al.*, 2012–2015) is, therefore, used for automated compensation of the tilt around ry_1 (the tilt around rx_1 is not compensated as its effect on the KB focusing is only of second-order). An inclinometer mounted on hexapod 1 with a sensitivity of 0.1 µrad is used as

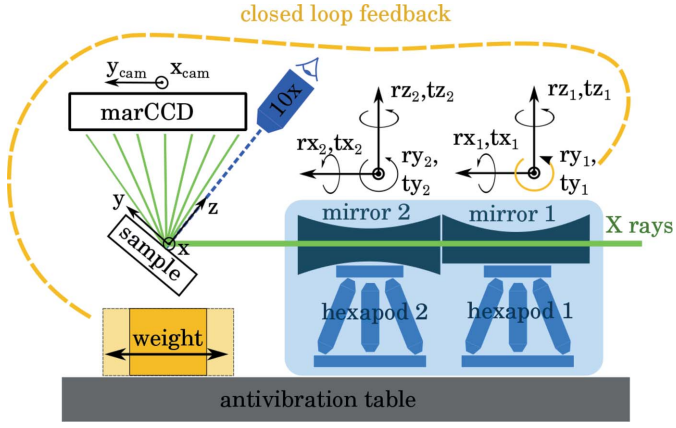

Figure 1
Schematic illustration of the Laue microdiffraction setup including an active and passive vibration-damping plate, which supports the sample scanning stages, the hexapods carrying the KB mirrors and the retractable optical microscope. The tilt inclinometer mounted on hexapod 1 monitors the tilt of the first mirror around ry_1 (*i.e.* the incident angle). A linear stage along the tx_1 direction carrying a 3 kg mass serves as a tilt actuator to compensate unwanted variations of the tilt. In the alignment phase, for accurate sample positioning, a retractable motorized optical microscope with 0.5 µm resolution, in-line illumination and a zoom-adjustable field of view from 38 to 200 µm replaces the retractable motorized two-dimensional X-ray detector.

a sensor and a motorized linear stage carrying a 3 kg mass is used as an actuator. Except for temporary overshoots in reaction to microscope or sample displacements larger than 10 mm, the amplitude of the tilt variations around the setpoint remains below ± 0.2 µrad. This system limits 24 h drifts of the beam position with respect to the sample to <2 µm. Short-term (20 min) oscillations of the beam position are of the order of ± 50 nm, being linked to temperature oscillations of $\pm 0.05^{\circ}$C in the control of the air conditioning of the lead-shielded hutch containing the instrument.

The two-dimensional detector for recording the diffracted intensity is a MarCCD165 (165 mm diameter) with 2048 × 2048 pixels of 80 µm, mounted at 90° with respect to the incident beam, 70 mm away from the probe point on the sample, leading to a collection angle of approximately 100°. The collected Laue pattern typically features 100 spots for a germanium single-crystal.

2.2. KB scanning and *in situ* nanowire loading

Here, two types of motions of the KB mirrors are demonstrated for scanning the microbeam on the sample surface: (i) the angular method which uses the incident angle (ry_1 or rz_2), and (ii) the translation method which scans the vertical position of the mirror (normal to its surface, tz_1 or ty_2). For each of these scanning approaches, the beam-scanning pseudo-motor had to be calibrated by measuring the displacement of the X-ray beam on the sample surface as a function of the displacement of the hexapods carrying the KB mirrors. Besides this calibration, the effect of the microbeam displacement on the focal size had to be investigated. For this, sample-stage linear scans across either a 100 nm-diameter Au nanowire or 2 µm-wide copper lines (embedded in a trench patterned in an Si substrate resulting from a Damascene elaboration process) were performed for each position of the hexapod pseudo-motors. During these scans the gold or the copper fluorescence signals were monitored using a Röntec XFlash 1001 energy-resolved point detector. An optical micrograph of the copper lines and typical linear scans across such lines are presented in Figs. S2(*a*) and S2(*b*), respectively, of the online supporting information. The position and the size of the X-ray focal spot were deduced by fitting the line profiles by a slit function, built by convoluting a Gaussian beam with a gate function.

An alternative and faster method to calibrate the beam scanning pseudo-motors consists in imaging the micro-beam footprint on a 5 µm-thick fluorescent YAG crystal using the optical microscope. Immediate digital image processing analysis of the microscope images provides the x and the y positions of the beam as well as the FWHM in both lateral directions. With this second method, the beam position is measured in more realistic conditions, repeating hexapod motions with a high frequency, while the sample remains fixed. KB scans can also be easily repeated to test their reproducibility, using forward scans or backward scans to test the effect of the scanning direction. However, the beam size measured with this method (*via* the size of the visible spot) only gives indicative values owing to the limited optical resolution of the optical microscope.

One important question for the vertical KB-scans was the strategy for the tilt-feedback system. Indeed, each motion in tz_1 induces a temporary perturbation of ry_1, *i.e.* of the tilt angle. The observation of the beam spot on the YAG during the tz_1-scans showed that the spot stabilization after a motion in tz_1 was much faster in the absence of tilt feedback. This is due to the slower response of the inclinometer compared with the tz_1 motion. Stopping the tilt feedback is, therefore, desirable during tz_1-scans, to avoid an overshoot. On the other hand, the tilt feedback was desirable during the sample scans on the copper line used in the first tz_1-scan calibration method. The tilt feedback was, therefore, kept active during these measurements.

Once the beam scanning pseudo-motors were calibrated, beam mapping was applied to two nanowires: (1) a pristine nanowire was scanned in two dimensions using the 'translation method', and (2) an Au nanowire under load in a three-point bending configuration was scanned along its length using the 'angular method'. The single crystalline gold nanowires were prepared by physical vapor deposition on carbon-coated tungsten substrates (Richter *et al.*, 2009) and placed on Si micro-ridges forming suspended nano-bridges. A mechanical load was applied with the tip of the *in situ* AFM 'SFINX' (Ren *et al.*, 2014; Leclere *et al.*, 2015), which was installed on the sample stage of the Laue microdiffraction setup. By moving the AFM-tip downwards at a constant speed of 2 nm s^{-1}, which presses the tip against the nanowire, the wire was deformed mechanically. The tip motion was interrupted at several stages for X-ray mapping. A typical Laue microdiffraction pattern taken with the X-ray beam on the nanowire is presented in Fig. S3 of the online supporting information. It shows the intense Laue pattern from the Si substrate and the weaker Laue pattern from the wire, consisting of about 20 spots.

3. Results and discussion

3.1. Beam displacement calibration

For calibration, the displacement of the focal spot on the sample surface and the FWHM of the beam focus were determined as a function of the rotation angle or of the lateral displacement of the mirrors (tz_1 or ty_2). For each angular step of $\Delta rz_2 = 0.005^{\circ}$ or lateral step of Δtz_1 and Δty_2 of 0.5 µm and, thus, each displacement of the beam on the sample, the calibration sample was scanned through the focal spot employing the motors of the sample stage itself. The beam position on the sample, the FWHM of the focus, the beam intensity and the error in the beam position with respect to a linear function are presented in Fig. 2 as a function of rz_2, tz_1 and ty_2. When rotating the downstream mirror the displacement of the beam focus on the sample surface is directly proportional to the rotation angle with a calibration factor $dx/drz_2 = 223$ µm per degree. However, a −5 µm (+5 µm) beam displacement increases the horizontal beam size from 800 to 1200 nm

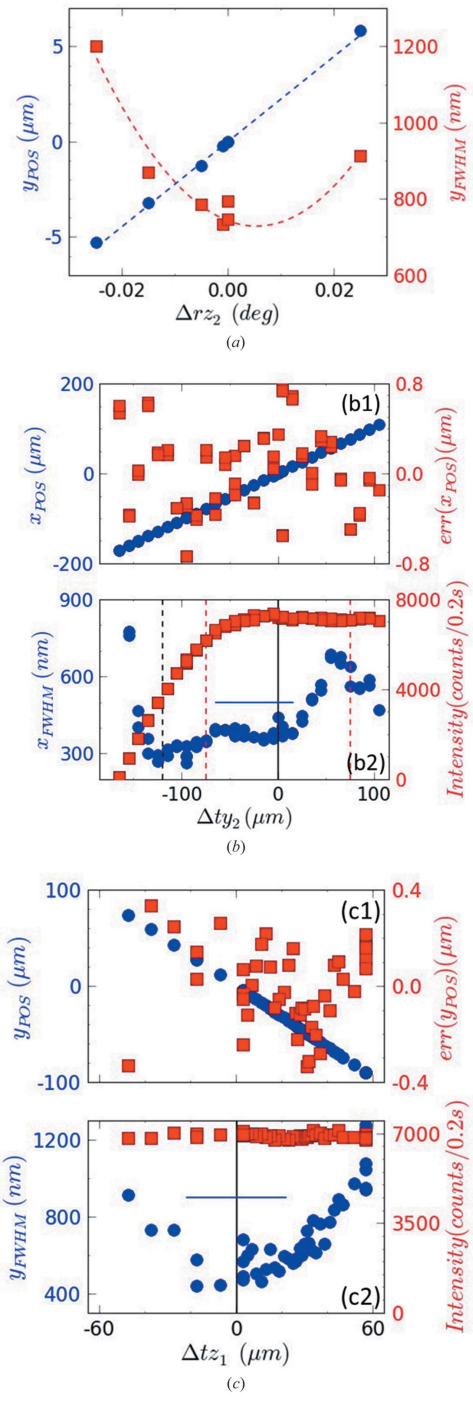

Figure 2
Calibration curves for the beam scanning pseudo-motors. (*a*) Angular method: displacement and full width at half-maximum (FWHM) of the beam focus on the sample surface as a function of the rotation of the downstream mirror. (*b*) and (*c*) Translation method: (*b*1) Micro-beam position in *x* direction (circles) and error on *x* position (squares) as a function of d(ty_2). (*b*2) Micro-beam size along *x* (circles) and intensity (squares) *versus* d(ty_2). The vertical red lines mark the edges of the beam impinging on the mirror at d(ty_2) = 0 (best focus). The mirror edges coincide with the slit center at d(ty_2) = −120 μm (black dashed vertical line) and d(ty_2) = +240 μm (out of the graph). The ty_2 scanning range with optimal beam properties (high intensity and small size) has a width of 80 μm as indicated by the blue horizontal line. (*c*1) Micro-beam position in *y* direction (circles) and error on *y* position (squares) as a function of d(tz_1). (*c*2) Micro-beam size along *y* (circles) and intensity (squares) *versus* the tz_1 offset of the first KB mirror. The tz_1 scan range with optimal beam size has a width of 40 μm as indicated by the blue horizontal line.

(950 nm). Here the sample used for calibrating the pseudo-motor was a flat-lying gold nanowire with a diameter of about 100 nm, oriented at 34° from the *y* axis. The gold fluorescence profiles were fitted with a Gaussian function, whose FWHM is shown in the figure. This FWHM is only indicative of the evolution of the beam size. Even for the best focus value of rz_2, it is significantly larger than the beam FWHM (450 nm) measured using a vertical copper line. This difference is most likely due to the angle between the wire and the *y* axis. The strong effect of the mirror rotation on the focal size is a drawback of the angular method. In contrast, the beam focus is well preserved in the translation method. Figs. 2(*b*1) and (*c*1) display the position of the microfocused beam in the *x* and in the *y* direction as a function of the lateral displacement of the mirrors by the hexapod pseudo-motors ty_2 and tz_1. The beam position in both directions can be well approximated by linear functions with slopes of 1.035 and −1.58. The errors with respect to the linear law are also presented in the figures. The FWHM of the beam in the two directions as well as the beam intensity are shown in Figs. 2(*b*2) and 2(*c*2). For the horizontal and the vertical motion of the beam, the horizontal and the vertical beam width remains below 400 nm over a range of 80 μm in ty_2 and below 500 nm over range of 40 μm in tz_1, respectively. The latter corresponds to a range of 60 μm on the sample surface due to the 50° tilt between the sample surface and the vertical direction. The beam intensity is unaffected by the lateral mirror displacements as long as the displacement stays within the area defined by the slits located in front of the focusing optics. The translation method allows for displacing the X-ray beam by several tens of micrometers on the sample surface while conserving both beam intensity and focal size. The scan range with optimal beam properties for the two directions is indicated by a blue line in each graph.

3.2. Application of KB scanning to the mapping of Au nanowires

3.2.1. Pristine Au nanowire imaged using the translation method. Figs. 3(*a*) and 3(*b*) present a two-dimensional map of the Au-L_{III} fluorescence yield and a mosaic of the Au 331 Laue spot, respectively, for a pristine Au nanowire lying on a flat Si substrate. The two maps were recorded simultaneously by scanning the two KB mirrors in steps of 0.5 μm in ty_2 and tz_1. The actual pixel size of the recorded two-dimensional maps on the sample surface is 0.5 μm in the horizontal and 0.75 μm in the vertical direction. Note that the vertical beam size is much larger than the nanowire diameter of ∼200 nm, thus dominating the observed width of the nanostructure.

3.2.2. Mechanically loaded suspended Au nanowire imaged using angular method. Prior to the mechanical loading of the suspended Au nanowire [see Fig. 4(*a*)] by SFINX, the AFM-tip, the nanowire of interest, and the focused X-ray beam were aligned with respect to each other as described by Leclere *et al.* (2015). At three deformation states the loading process was interrupted while maintaining the load, the X-ray beam was scanned along the deformed nanowire in steps of 500 nm using the angular method and

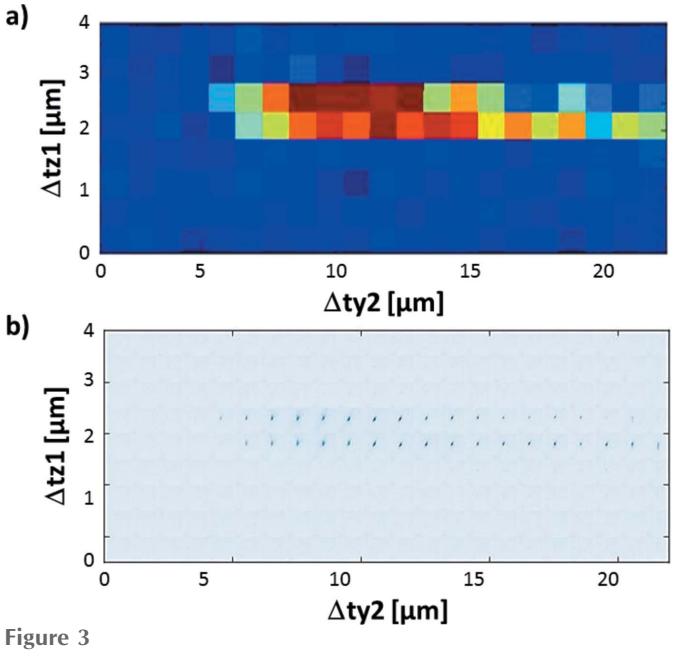

Figure 3
Two-dimensional maps of (*a*) the Au-L_{III} fluorescence yield and (*b*) the Au 331 Laue spot (box size: 100 × 100 pixels of the same area on the detector for all positions in the two-dimensional map) for a single Au nanowire on an Si substrate recorded by scanning the two KB mirrors in steps of 0.5 µm.

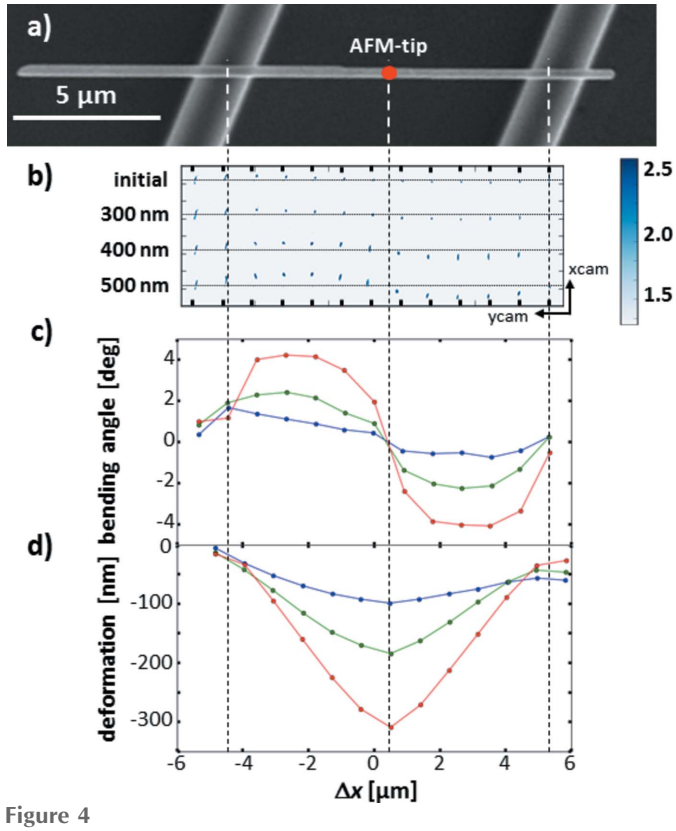

Figure 4
(*a*) Scanning electron microscopy image of a suspended Au nanowire resting on two 2 µm-wide Si ridges. (*b*) Mosaic of the Au 222 Laue spot along the nanowire for different loading stages (box size: 200 × 200 pixels on detector). (*c*) Bending angle along the nanowire calculated from the orientation matrices UB which were inferred from the position and displacement of at least eight Au Laue spots on the detector. (*d*) Vertical displacement along the nanowire for the different loading stages computed by integration of the bending angle curves shown in (*c*).

µLaue diffraction patterns were recorded. For simplicity the evolution of only one Laue spot, the Au 222 reflection, along the nanowire in the pristine state as well as for the three different deformation states is presented in Fig. 4(*b*). The boxes in the mosaic were rotated by 90° counter-clockwise with respect to the usual orientation for Laue patterns (here 2θ increases towards the left) in order to highlight the *xcam* component of the spot displacement, which is associated with the wire bending. The spot sequences reveal a sinusoidal behavior where the spot is displaced above and below the dotted lines which indicate the Laue spot position for a uniform orientation of the crystal lattice along the wire. The fact that the Laue spot for the pristine wire is displaced from its 'perfect' position indicates that the wire is slightly deformed before loading. The amplitude of the spot displacement increases with increasing displacement of the piezoelectric stage which carries the AFM cantilever.

A more quantitative analysis of the series of Laue patterns was performed using the *LaueTools* software (Micha, 2014). After determining the central positions of several Au spots within the Laue pattern, the orientation of the Au unit cell (three angles) as well as its shape (five lattice parameters: b/a, c/a, α, β, γ) were refined. This refinement is based both on the positions of at least eight indexed Au Laue spots and on the calibration of the experimental geometry obtained from the positions of the Si substrate Laue spots. Owing to the fact that the X-ray beam passes through the complete thickness of the bent wire, *i.e.* a part which is under compression, a part under tension as well as the neutral axis in between the two strained zones, the mean strain ε_{xx} is of the order of zero. Therefore, the Laue patterns were fitted using a fixed cubic shape of the Au unit cell leaving only the crystal orientation as a free parameter. From the obtained orientation (UB) matrices, the variation of the three principal angles (*i.e.* the total misorientation angle with respect to the crystal orientation at the left end of the wire) of the crystal lattice was inferred from which the bending angle of the nanowire was deduced.

The bending angle along the nanowire for the three deformed states is presented in Fig. 4(*c*), revealing a sinusoidal behavior similar to the sinusoidal displacement of the Au 222 Laue spot on the detector. At both ends of the wire as well as below the tip, the bending angle remains close to 0° even for the largest load. The symmetry of the nanowire profile demonstrates that the load is applied in the center of the suspended nanowire. Halfway between the loading point and the supports the bending angle increases to up to 4°. From the bending angle the nanowire shapes were computed and are displayed (vertically exaggerated) in Fig. 4(*d*). The nanowire deflection at the center (80, 135 and 190 nm) can then be compared with the displacement of the piezoelectric stage carrying the tip after the tip has been in contact with the nanowire (100, 200 and 290 nm). From the difference between the movement of the piezoelectric stage and the nanowire deformation, the deflection of the cantilever is inferred which

eventually allows for determining the actual applied force. Taking into account the stiffness of the AFM cantilever of 5 N m^{-1}, the applied force for the three deformation states amounts to 100, 325 and 500 nN. The difference of 50 nm at the right end of the nanowire between the first and the second loading stage is considered as non-significant as it is below the cumulated uncertainties of the 12 orientation matrices. Besides the deflection the nanowire profile also allows for the determination of the boundary conditions, *i.e.* whether the wire is thoroughly clamped or simply supported. The analytical solutions for the shape and the bending angle profiles for the two cases are presented in Fig. S5 of the online supporting information. The comparison of these analytical solutions with the experimentally obtained profiles clearly confirms the validity of the doubly clamped hypothesis [used by Leclere *et al.* (2015)]. The determination of the boundary conditions is of major importance for the interpretation of the mechanical behavior of a mechanically loaded structure.

4. Conclusion

In conclusion, a new *in situ* mapping technique was presented where the sub-micrometer focused polychromatic X-ray beam is scanned across the stationary sample surface by translating the KB focusing mirrors mounted on hexapods instead of *xy* scanning the sample with respect to the fixed incident beam. The capabilities of this new method were demonstrated by recording μLaue diffraction patterns along an *in situ* mechanically loaded suspended Au nanowire. This *in situ* measurement gave access to the complete nanowire profile at different loading stages and further allowed for determining the boundary conditions of the suspended structure. These boundary conditions are of major importance for the understanding of the mechanical behavior.

This new scanning technique is of interest to a broad scientific community by paving the way to map whole structures *in situ* in cases where sample movements may interfere with the measurement (*e.g.* mechanical test) and, thus, conventional experiments are limited to one single position on the sample.

Acknowledgements

The authors gratefully acknowledge the financial support from the French National Research Agency through the project ANR-11-BS10-01401 MecaniX. They further thank the French CRG program committees for the allocated beamtime at the BM32 beamline at ESRF.

References

Chen, L. Y., Richter, G., Sullivan, J. P. & Gianola, D. S. (2012). *Phys. Rev. Lett.* **109**, 125503.
Chung, J.-S. & Ice, G. E. (1999). *J. Appl. Phys.* **86**, 5249.
Jefimovs, K., Bunk, O., Pfeiffer, F., Grolimund, D., van der Veen, J. F. & David, C. (2007). *Microelectron. Eng.* **84**, 1467–1470.
Kiener, D., Grosinger, W., Dehm, G. & Pippan, R. (2008). *Acta Mater.* **56**, 580–592.
Kirchlechner, C., Imrich, P. J., Grosinger, W., Kapp, M. W., Keckes, J., Micha, J. S., Ulrich, O., Thomas, O., Labat, S., Motz, C. & Dehm, G. (2012). *Acta Mater.* **60**, 1252–1258.
Kirkpatrick, P. & Baez, A. V. (1948). *J. Opt. Soc. Am.* **38**, 766–774.
Konijnenberg, P. J., Zaefferer, S. & Raabe, D. (2015). *Acta Mater.* **99**, 402–414.
Leclere, C., Cornelius, T. W., Ren, Z., Davydok, A., Micha, J.-S., Robach, O., Richter, G., Belliard, L. & Thomas, O. (2015). *J. Appl. Cryst.* **48**, 291–296.
Lee, S., Im, J., Yoo, Y., Bitzek, E., Kiener, D., Richter, G., Kim, B. & Oh, S. H. (2014). *Nat. Commun.* **5**, 3033.
Maaß, R., Van Petegem, S., Borca, C. N. & Van Swygenhoven, H. (2009). *Mater. Sci. Eng. A*, **524**, 40–45.
Marichal, C., Van Swygenhoven, H., Van Petegem, S. & Borca, C. (2013). *Sci. Rep.* **3**, 2547.
Micha, J.-S. (2014). *LaueTools: Open Source Python Packages for X-ray MicroLaue Diffraction Analysis*, http://sourceforge.net/p/lauetools/lauetoolswiki/Home.
Ren, Z., Mastropietro, F., Davydok, A., Langlais, S., Richard, M.-I., Furter, J.-J., Thomas, O., Dupraz, M., Verdier, M., Beutier, G., Boesecke, P. & Cornelius, T. W. (2014). *J. Synchrotron Rad.* **21**, 1128–1133.
Richter, G., Hillerich, K., Gianola, D. S., Mönig, R., Kraft, O. & Volkert, C. A. (2009). *Nano Lett.* **9**, 3048–3052.
Rodrigues, M. S., Cornelius, T. W., Scheler, T., Mocuta, C., Malachias, A., Magalhães-Paniago, R., Dhez, O., Comin, F., Metzger, T. H. & Chevrier, J. (2009). *J. Appl. Phys.* **106**, 103525.
Scheler, T., Rodrigues, M., Cornelius, T. W., Mocuta, C., Malachias, A., Magalhães-Paniago, R., Comin, F., Chevrier, J. & Metzger, T. H. (2009). *Appl. Phys. Lett.* **94**, 023109.
Snigirev, A., Kohn, V., Snigireva, I. & Lengeler, B. (1996). *Nature (London)*, **384**, 49–51.
Uchic, M. D., Dimiduk, D. M., Florando, J. N. & Nix, W. D. (2004). *Science*, **305**, 986–989.
Ulrich, O., Biquard, X., Bleuet, P., Geaymond, O., Gergaud, P., Micha, J. S., Robach, O. & Rieutord, F. (2011). *Rev. Sci. Instrum.* **82**, 033908.
Ulrich, O., Micha, J.-S., Robach, O., Biquard, X., Tardif, S. & Rieutord, F. (2012–2015). *Upgraded Laue microdiffraction setup on the CEA-CNRS CRG-IF BM32 beamline at ESRF. BM32 Beamline Annual Reports 2012–2015.* ESRF. Grenoble, France.